Toward Non-Invasive Calibration-Free Blood Pressure Estimation: A Physics-Informed Neural Network with Hemodynamic Priors

Toward Non-Invasive Calibration-Free Blood Pressure Estimation: A Physics-Informed Neural Network with Hemodynamic Priors

Federico Delrio, Vincenzo Randazzo, Giansalvo Cirrincione, Eros Pasero

***Abstract*— Continuous and calibration-free arterial blood pressure (ABP) monitoring remains a major challenge in wearable sensing. Most data-driven estimators rely on ECG–PPG correlations without enforcing the underlying cardiovascular physics, which limits its interpretability and cross-subject generalization. We introduce a hemodynamics-driven Physics-Informed Neural Network (PINN) that reconstructs the full radial pressure waveform from ECG and fingertip PPG. The model embeds a 1D pulse-wave propagation PDE, Windkessel boundary conditions, and spatially varying vessel geometry and physiology, treated as soft physiological constraints. Trained on MIMIC III database and evaluated on the large clinical database VitalDB, the model achieved an inter-subject MAE of 13.10 mmHg, with SBP 15.84 mmHg and DBP 10.42 mmHg. Beyond waveform reconstruction, the framework predicts also additional hidden physiological quantities, such as radius and wall thickness, elasticity, flow and spatial pressure evolution, consistently with the governing equations. These results highlight both the promise and the current limitations of physics-informed modeling, positioning this work as a foundational step toward future personalized, physiologically grounded, and calibration-free cuffless BP monitoring, while remaining not ISO 81060-2 compliant or clinically deployable in its current form.**

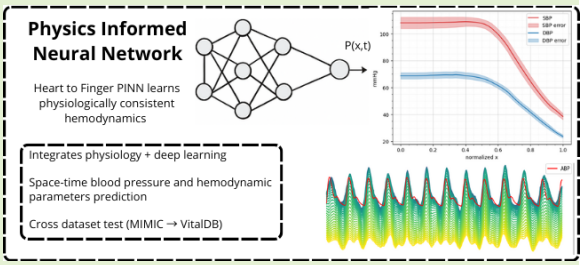

***Index Terms*— Blood Pressure Estimation, Cuffless Monitoring, ECG, Hemodynamics, Physics-Informed Neural Networks, PPG**

I. Introduction

BLOOD pressure (BP) is a key cardiovascular vital sign, and hypertension remains a major global risk factor for stroke, myocardial infarction, and kidney disease [1]. Yet cuff-based devices provide only intermittent measurements and are inconvenient for long-term use [2]. This has motivated cuffless BP estimation from electrocardiogram (ECG) and photoplethysmogram (PPG) signals, which are naturally compatible with wearable sensing [3]–[11].

Two main paradigms have been pursued, each with clear limitations. *Data-driven* methods can map waveform morphology to BP effectively within a dataset, but often generalize poorly because they learn correlations rather than mechanisms [12]–[16]. *Model-based* methods offer interpretability and physical consistency, but usually require subject-specific calibration and remain too rigid for wearable deployment [17]. Bridging these paradigms while preserving calibration-free operation remains an open challenge [18], [19].

The principle of combining data-driven representations with domain-specific model constraints has proven effective across several engineering fields. In power-system control, hybrid model-informed neural architectures have been used for reliable virtual synchronous generator design [20] and for analysing oscillation transfer mechanisms in grid-forming converters [21], where the physics of the synchronous machine provides hard constraints on the learning problem. In graph-based cybersecurity, learned sub-graph representations have been combined with structural priors to detect smart-contract vulnerabilities [22]. In each case, the key insight is that purely data-driven models lack the inductive bias needed for reliable out-of-distribution generalisation, while purely rule-based models lack the flexibility to adapt to real-world variability.

We do not claim a clinically deployable estimator. Our aim is instead to test whether embedding mechanistic hemodynamics into a neural network can produce physiologically consistent pressure waveforms and improve robustness relative to purely data-driven models. This study extends our previous PINN-based work toward a more complete and physiologically grounded formulation [23].

The specific contributions of this work are:

1) **Heart-to-finger hemodynamic PINN formulation.** We

Delrio acknowledges Eurecom for support in his PhD research. During the preparation of this work the authors used ChatGPT to shorten some sections and, above all, to improve the english fluency. After using this tool, the authors carefully reviewed and edited the content as needed and take full responsibility for the content of the publication.

F. Delrio, V. Randazzo, and E. Pasero are with Politecnico di Torino, DET Department, Turin, Italy (email: federico.delrio@polito.it, vincenzo.randazzo@polito.it)

G. Cirrincione is with University of Picardie Jules Verne, Amiens, France

propose a PINN that couples 1D pulse-wave propagation with a three-element Windkessel model to reconstruct the radial pressure waveform from ECG and fingertip PPG without per-subject cuff calibration.

2) **Spatially varying physiological parameterisation.** Vessel geometry, elasticity, viscosity, and terminal impedance are treated as learnable distributed quantities constrained by soft physiological priors.
3) **Latent physiological variable reconstruction.** Beyond BP estimation, the framework infers hidden quantities such as flow, compliance, wall stiffness, and spatial pressure evolution.
4) **Large-scale cross-database evaluation.** The model is trained on MIMIC-III and evaluated under subject-disjoint conditions on VitalDB to characterize both the promise and the limitations of physics-informed BP estimation.

II. State of the Art

Early ECG–PPG BP estimators were largely data-driven, using convolutional or recurrent models to map waveform morphology directly to BP [7], [24]–[26]. Although accurate within a dataset, they often generalize poorly across subjects and databases [18], [27], [28]. To address this, recent work has embedded physiological structure through PINNs and related operator-based models, including BP-DeepONet and physics-informed temporal networks [29]–[32]. A closely related concurrent study by Crandall et al. [33] further supports the relevance of physics-informed calibration-free monitoring. Building on these directions, we combine 1D blood-flow equations with Windkessel termination in a single framework trained on MIMIC-III and evaluated on VitalDB.

III. PPG link to blood flow and blood pressure

The key idea is simple: PPG captures pulsatile blood-volume changes, mass conservation links those changes to flow, and local compliance links flow to pressure. We use this minimal chain only to justify the weak distal calibration adopted by the PINN.

A. From Beer–Lambert Law to a Linear $\mathrm{PPG} \sim \mathrm{V_b}$ Model

After standard conditioning and DC removal, the pulsatile PPG component can be approximated as proportional to the local arterial blood volume,

$$\mathrm{PPG}_{AC}(t) \;\propto\; V_b(t), \tag{1}$$

which, under a local linear compliance assumption, leads to the approximate relation

$$p(t) \;\propto\; \mathrm{PPG}(t). \tag{2}$$

This relation is used only as a weak distal observational anchor, while the full pressure field is constrained by the embedded hemodynamic equations.

IV. Physics-Based 1D Hemodynamics with Windkessel Termination

To describe the propagation of the arterial pressure wave from the aortic root to the fingertip, we employ the one-dimensional (1D) blood flow equations derived from mass and momentum conservation, following [31]. The governing system is

$$\frac{\partial A}{\partial t} + \frac{\partial Q}{\partial x} = 0, \tag{3}$$

$$\frac{\partial Q}{\partial t} + \frac{\partial}{\partial x}\left(\frac{Q^2}{A}\right) + \frac{A}{\rho}\frac{\partial p}{\partial x} + K_r\frac{Q}{A} = 0, \tag{4}$$

where $Q(x,t)$ is volumetric flow, $A(x,t)$ is vessel cross-sectional area, $p(x,t)$ is pressure, ρ is blood density, and K_r is an effective viscous/friction parameter.

To close the system, a pressure–area constitutive law is required. A common linear elastic approximation is

$$p(x,t) = p_0 + \frac{\beta}{A_0}\big(A(x,t) - A_0\big), \tag{5}$$

where A_0 is the reference cross-sectional area at diastolic pressure p_0, and β is the stiffness coefficient related to vessel elasticity and wall thickness.

The downstream load at $x = L$ is represented using a three-element Windkessel model, consisting of a proximal resistance R_1, a compliance C, and a distal resistance R_2. This yields the equivalent boundary equation:

$$Q(L,t)\left(1 + \frac{R_1}{R_2}\right) + CR_1\frac{dQ(L,t)}{dt} + \frac{p(L,t)}{R_2} - C\frac{dp(L,t)}{dt} = 0. \tag{6}$$

In our formulation, the outlet $x = L$ is explicitly chosen as the fingertip, i.e. immediately proximal to the capillary bed. In this setting, R_2 captures the microvascular resistance of the distal network, while C represents the compliance of the local arteriolar bed. The Windkessel condition thus acts as the interface between macrocirculatory wave propagation (governed by (3)–(5)) and the dissipative microcirculation, ensuring that the predicted distal pressure waveform reflects both upstream reflections and downstream damping.

V. Physiological Parameterization and Constraints

To constrain the PINN to physiologically plausible regimes while preserving subject-specific adaptability, we impose *soft* priors on a limited set of parameters appearing in the 1D hemodynamic equations and in the Windkessel termination. These include blood density ρ, reference cross-sectional area $A_0(x)$, pressure–area coupling $\beta(x)$, distributed viscous/friction term $K_r(x)$, and terminal elements (R_1, R_2, C), all defined with respect to a baseline pressure p_0 and external pressure P_{ext}. Priors are implemented as quadratic penalties around nominal profiles or ranges rather than as hard constraints, allowing the model to adapt to inter-subject variability. The spatial coordinate $x \in [0,1]$ denotes the normalized path from the aortic root ($x = 0$) to the fingertip ($x = 1$).

Nominal trends for vessel radius, wall thickness, elasticity, and viscosity are drawn from established hemodynamic

literature [34]–[36]. Although not derived from a unified meta-analysis, these priors consistently encode well known qualitative behaviors: arterial tapering toward the periphery, decreasing wall thickness, increasing stiffness with decreasing radius, and viscosity variations consistent with the Fåhræus–Lindqvist effect. In this framework, such priors act as soft physiological regularizers rather than exact anatomical prescriptions, preventing non physical solutions while retaining sufficient flexibility for subject-specific adaptation. For reference, blood density is anchored around $\rho \simeq 1060\ \mathrm{kg\,m^{-3}}$.

Table I summarises the nominal ranges and penalty centres used for each physiological parameter. All penalties are implemented as squared deviations from the nominal value, weighted by the corresponding λ_{reg} coefficient in the composite loss (Eq. 12)

.

TABLE I
NOMINAL RANGES AND PRIOR CENTRES FOR THE PHYSIOLOGICAL PARAMETERS USED AS SOFT REGULARISERS IN THE PINN. VALUES ARE DRAWN FROM [30], [34]–[36].

Parameter	Nominal range / centre	Source
Blood density ρ	$1060\ \mathrm{kg\,m^{-3}}$	[34]
Aortic radius $R_0(0)$	12–15 mm	[36]
Fingertip radius $R_0(1)$	0.5–1.5 mm	[36]
Wall thickness $h_0(0)$	1.5–2.5 mm	[36]
Young's modulus E (aorta)	0.4–0.8 MPa	[37]
Young's modulus E (digital)	1.5–3.0 MPa	[37]
Proximal resistance R_1	$0.05–0.1\ \mathrm{mmHg\,s\,ml^{-1}}$	[30]
Distal resistance R_2	$0.5–1.5\ \mathrm{mmHg\,s\,ml^{-1}}$	[30]
Compliance C	$1.0–2.0\ \mathrm{ml\,mmHg^{-1}}$	[30]
Baseline pressure p_0	60–80 mmHg	clinical range

A. Modeling of $A_0(x)$ (radius–based fit)

The reference lumen area profile $A_0(x)$ and arterial wall thickness $h_0(x)$ were obtained from nominal anatomical values reported for large and medium arteries from different sources, spanning the aorta, subclavian, brachial, radial/ulnar, and digital branches [36]. Smooth fitted functions $R_0(x)$ and $h_0(x)$ were constructed to capture the gradual tapering and thinning observed along this arterial pathway.The radius and thickness fits are shown in Fig. 1.

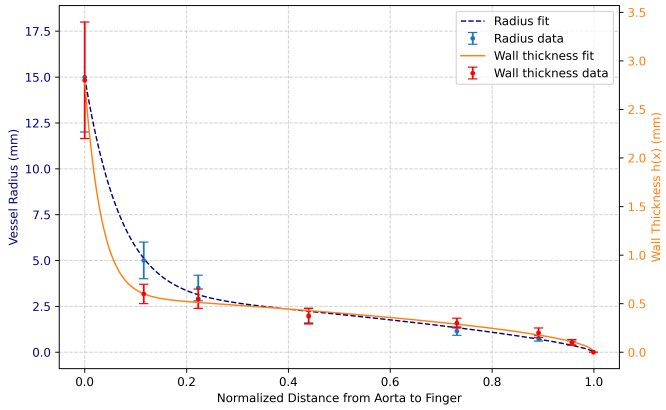

Fig. 1. Radius profile (dark blue) and wall-thickness (orange) used as physiological prior

B. Elasticity and the pressure–area coupling $\beta(x)$

The elastic response of the arterial wall enters the 1D hemodynamic model through the pressure–area constitutive law, which requires a coupling coefficient

$$\beta(x) \;=\; \sqrt{\pi}\,E(x)\,h_0(x), \tag{7}$$

with $E(x)$ the effective Young's modulus of the wall and $h_0(x)$ the local thickness. A major source for such parametrizations is the work of Stergiopulos et al. [38], who compiled and fitted data originally presented by McDonald [39], Caro et al. [40], and Langewouters et al. [37].

Their regression produced the widely adopted relation

$$E(r_0) \;=\; k_1 \exp(k_2 r_0) + k_3, \tag{8}$$

with constants:

$$(k_1, k_2, k_3) = (1.89 \times 10^7,\ -18.34,\ 3.53 \times 10^6) \tag{9}$$

This relation captures the fact that larger arteries (e.g. aorta) are more compliant (lower E) while distal arteries are stiffer, consistent with in vivo observations. More details can be found from the work of Mette Sophie Olufsen [36].

C. Distributed viscous losses and the parameter $K_r(x)$

Energy dissipation along the arterial tree is modeled by the distributed resistance term $K_r(x)$ appearing in the momentum equation. While large-artery wave propagation is mainly governed by compliance and inertia, friction becomes increasingly relevant in the distal segments, where vessel diameters fall below a few millimeters. Following again the work of of Pries, Neuhaus, and Gaehtgens [35], we have that:

$$K_r(x) \;=\; \frac{8\pi\,\mu(x)}{\rho}\ mmHg, \tag{10}$$

where $\mu(x)$ is the apparent viscosity of the plasma.

VI. NEURAL NETWORK ARCHITECTURE

A. Principle of the neural network for blood pressure evaluation

In purely data-driven approaches, the network learns a direct nonlinear mapping from ECG and PPG morphology to BP, encoding statistical correlations present in the training data rather than the physical mechanisms that generate the pressure waveform. In the proposed PINN, by contrast, the network solves an *inverse hemodynamic problem*: from $(x, \mathrm{ECG}, \mathrm{PPG})$ it estimates the parameter set $\boldsymbol{\theta} = (\rho, K_r, \beta, A_0, R_1, R_2, C, p_0, p_{ext}, \alpha, Q_s, Q_{off})$ together with the fields $p(x,t)$ and $Q(x,t)$. The BP waveform is therefore a consequence of the governing physics evaluated with the estimated parameters, not a direct regression target.

B. Coupling between the neural network and the physics model

The neural network and the physics model are coupled at two levels.

Parameter-level coupling: the parameter layer outputs $\boldsymbol{\theta}$, which directly populates the coefficients of Eqs. 3–6.

Residual-level coupling: the prediction head outputs $p(x,t)$ and $Q(x,t)$, which are fed back into the governing equations to compute the PDE and Windkessel residuals appearing in the loss. Data select a solution from the feasible set, while physics defines feasibility; neither component is sufficient alone.

The input consists of the normalized spatial coordinate $x \in [0,1]$, an ECG segment, and a synchronized PPG segment. Each example is an 8-second window (1000 samples at 125 Hz). A summary of the network is shown in Fig. 2

.

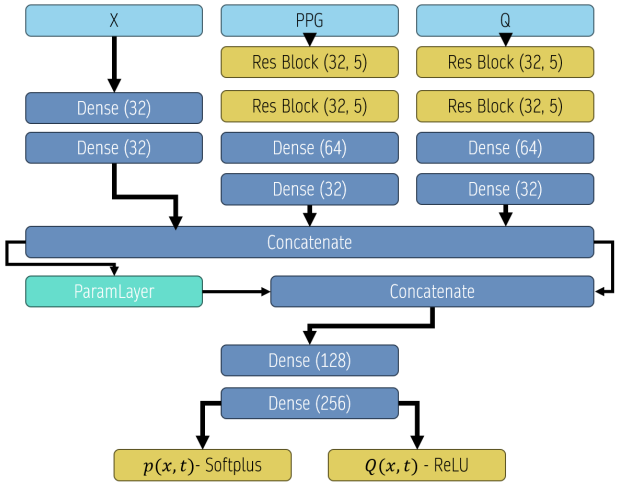

Fig. 2. Neural network structure in detail.

The ECG and PPG signals are processed by two residual 1D-CNN branches that extract waveform descriptors and project each signal to a 32-dimensional latent embedding. The spatial input x is processed through a small dense branch so that the network remains aware of propagation distance.

After concatenation, the three embeddings form a 96-dimensional feature vector processed by a compact parameter layer that outputs 12 scalars governing the PDE system, the Windkessel termination, and the distal PPG–pressure calibration.

Most physiological parameters and priors were introduced in Sec.V; here we specify the remaining scalars. We model the fingertip pressure as

$$p(L,t) \;=\; p_0 \;+\; \alpha\,\mathrm{PPG}(t), \tag{11}$$

where p_0 is the baseline offset and α is a linear gain linking predicted pressure to local PPG morphology. The external reference pressure p_{ext} appears in the p–A law and is kept learnable with weak regularization.

To map the inflow surrogate to a plausible aortic boundary, we use two calibration scalars: Q_s rescales its amplitude and Q_{off} corrects the baseline. This provides minimal flexibility without overriding the physics constraints.

C. Prediction head.

The fused features and parameter estimates are propagated through fully connected layers and finally output the predicted fields $p(x,t)$ and $Q(x,t)$. These fields are used for supervision and for the physics residuals.

D. Collocation sampling.

To enforce the PDE constraints, collocation points are sampled only in space because time is already encoded by the ECG and PPG windows. For each 8-second segment we sample $x_n \in [0,1]$, always including $x=0$, $x=0.5$, and $x=1$. The midpoint is supervised against invasive ABP, while derivatives for the PDE residuals are obtained by automatic differentiation in Keras/TensorFlow.

VII. Loss Function

Training is performed by minimizing a composite loss that combines data supervision, physics-based constraints, and physiological regularization. For each ECG/PPG window ($T=1000$ samples, 8 s) and a set of spatial collocation points $x_n \in [0,1]$ (including $x=0$, 0.5, and 1), the total loss is

$$\mathcal{L}_{\mathrm{tot}} = \sum_{k\in\mathcal{K}} \lambda_k\,\mathcal{L}_k, \qquad \mathcal{K} = \{\mathrm{ABP},\mathrm{PPG},\mathrm{PDE},\mathrm{WK},Q,\mathrm{reg}\}, \tag{12}$$

where λ_k denote scalar weighting coefficients balancing data supervision, physics informed constraints, and physiological regularization terms.

Ground-truth arterial blood pressure is enforced at a single virtual observation point ($x=0.5$),

$$\mathcal{L}_{\mathrm{ABP}} = \big\langle \big(p(0.5,t) - \mathrm{ABP}(t)\big)^2 \big\rangle, \tag{13}$$

anchoring the reconstructed waveform to invasive measurements without prescribing the full spatial field.

At the distal site ($x=1$, fingertip), the predicted pressure is softly aligned to the optical signal,

$$\mathcal{L}_{\mathrm{PPG}} = \big\langle \big(p(1,t) - (p_0 + \alpha\,\mathrm{PPG}(t))\big)^2 \big\rangle, \tag{14}$$

where p_0 and α are learned per window. This term acts as a distal observational anchor: it links the fingertip pressure to the local optical waveform without overriding the PDE dynamics.

Conservation of mass and momentum is enforced by penalizing the residuals of the 1D hemodynamic equations at all collocation points,

$$\mathcal{L}_{\mathrm{PDE}} = \big\langle r_1(x,t)^2 + r_2(x,t)^2 \big\rangle, \tag{15}$$

where $r_1 = \partial_t A + \partial_x Q$ is the continuity residual and $r_2 = \partial_t Q + \partial_x(Q^2/A) + (A/\rho)\,\partial_x p + K_r\,Q/A$ is the momentum residual. Minimizing $\mathcal{L}_{\mathrm{PDE}}$ enforces the 1D equations throughout the vessel, not only at the supervised point.

Physiological terminal loading is imposed through a three-element Windkessel boundary condition at the fingertip ($x=1$),

$$\mathcal{L}_{\mathrm{WK}} = \big\langle \mathrm{WK}(p,Q) \big\rangle^2, \tag{16}$$

where $\mathrm{WK}(p,Q)$ is the residual of Eq. 6 at $x=1$. Here R_1 represents the characteristic impedance of the terminal

arterioles, C the compliance of the local arteriolar bed, and R_2 the overall peripheral capillary resistance. This term ensures that the predicted distal pressure–flow relationship is consistent with microvascular physics, preventing non-physiological wave reflections at the outlet. Together, $\mathcal{L}_{\mathrm{PPG}}$, $\mathcal{L}_{\mathrm{PDE}}$, and $\mathcal{L}_{\mathrm{WK}}$ link the solution to the optical observation, the interior equations, and the terminal boundary condition.

Since inflow is not directly observed, the latent flow variable is weakly guided by the temporal structure of the PPG upstroke,

$$\mathcal{L}_Q = \left\langle \left(Q - q_{\mathrm{PPG}}\right)^2 \right\rangle, \tag{17}$$

together with admissibility penalties discouraging negative flow and large offsets. Finally, soft physiological priors constrain geometry, elasticity, resistance, density, and baseline pressure toward nominal ranges (Sec. V),

$$\mathcal{L}_{\mathrm{reg}} = \mathcal{L}_{A_0} + \mathcal{L}_{\beta} + \mathcal{L}_{K_r} + \mathcal{L}_{\rho} + \mathcal{L}_{p_0}, \tag{18}$$

preventing convergence to non-physical solutions while preserving subject-specific adaptability.

VIII. Training Strategy

Training data were drawn from two complementary sources: the MIMIC-III Waveform Database and the VitalDB subset distributed within PulseDB.

From MIMIC-III we selected records containing synchronous ECG (lead II), peripheral PPG (PLETH), and invasive ABP sampled at 125 Hz. Signals were segmented into fixed 8 s windows (1000 samples). A compact quality-control (QC) pipeline adapted from [7] removed segments with missing samples, saturation, baseline drift, abnormal amplitude ranges (ABP outside 15–300 mmHg), or inconsistent beat morphology. After filtering, 36 080 valid windows were retained.

To reduce subject-specific bias, extraction was limited to at most 10 windows per record. Because MIMIC-III does not provide explicit subject identifiers, windows from the same patient may still appear across dataset splits, potentially inflating apparent generalization performance.

For cross-database evaluation we used the VitalDB subset of PulseDB. The same ECG/PPG QC pipeline was applied, removing approximately 60% of corrupted windows and yielding about 170 000 valid segments (8 s ECG, PPG, ABP) across 1216 subjects. Unlike MIMIC-III, VitalDB provides explicit subject separation, enabling stricter evaluation of cross-patient generalization. Due to differences in acquisition protocols and population characteristics between the databases, performance degradation is expected when transferring the model trained on MIMIC-III.

a) Batching and collocation.: Training batches are formed by selecting ECG–PPG windows (8 s, 1000 samples) and augmenting each with N_x collocation coordinates $x_n \in [0, 1]$ sampled uniformly, with fixed inclusion of $x{=}0$, $x{=}0.5$, and $x{=}1$. Each batch therefore contains $B = M \times N_x$ triads $(x_n, \mathrm{ECG}, \mathrm{PPG})$. Supervised ABP labels are applied only at $x{=}0.5$, while the distal PPG anchoring term uses $x{=}1$. Physics residuals are evaluated at all collocation points.

b) Loss weighting.: The coefficients λ_k in Eq. 12 balance the loss components and are reported in Table II. The ABP supervision term ($\lambda_{\mathrm{ABP}}{=}1.0$) defines the reference scale. PDE and Windkessel residuals are initially down-weighted to avoid dominating early training and are increased during a 10-epoch warm-up. Regularization weights remain small to allow subject-specific adaptation while constraining parameters within physiological ranges.

TABLE II
LOSS WEIGHTING COEFFICIENTS λ_k USED IN THE COMPOSITE LOSS (EQ. 12) FOR ALL EXPERIMENTS.

Term	λ_k	Role
$\mathcal{L}_{\mathrm{ABP}}$	1.0	ABP supervision at $x{=}0.5$
$\mathcal{L}_{\mathrm{PPG}}$	0.5	Distal PPG anchor at $x{=}1$
$\mathcal{L}_{\mathrm{PDE}}$	0.1	Mass + momentum residuals
$\mathcal{L}_{\mathrm{WK}}$	0.1	Windkessel boundary condition
$\mathcal{L}_Q$	0.05	Flow surrogate guidance
$\mathcal{L}_{\mathrm{reg}}$	0.01	Physiological parameter priors

c) Optimization details.: Models were trained in TensorFlow/Keras using the Adam optimizer (learning rate 10^{-3}, $\beta_1{=}0.9$, $\beta_2{=}0.999$). Mixed-precision arithmetic was enabled to reduce memory usage and accelerate training. Batch size was 64 collocation triads. Gradients were backpropagated through both the feature extractors and the physics-informed parameter layer, with spatial derivatives computed via automatic differentiation.

d) Regularization and early stopping.: Dropout (0.1) was applied across convolutional and dense layers. Instead of weight decay, regularization relied on the physiological priors described in Sec. VII. Early stopping monitored the validation ABP error at $x{=}0.5$.

IX. Training

The first experiments were conducted on MIMIC-III, split into 80% training, 10% validation, and 10% testing. Because subject identifiers are unavailable, the split is window-level and may therefore overestimate generalization. Training ran for up to 100 epochs with early stopping.

On the held-out MIMIC-III test set, the model achieved a waveform MAE of 5.77 mmHg at the virtual mid-point observation, with SBP and DBP errors of 7.32 mmHg and 5.12 mmHg. These results are below clinical requirements and are not our best absolute MIMIC-III results [7], but they support the intended proof of concept: trading some raw accuracy for physiological interpretability and potentially improved generalization.

A. VitalDB

To evaluate cross-database generalization, the MIMIC-III model was first applied directly to the VitalDB subset of PulseDB, yielding a waveform MAE of 17.02 mmHg (SBP 19.19 mmHg, DBP 13.95 mmHg). This degradation reflects the expected shift in hardware, population, and recording conditions.

Transfer learning was then performed on VitalDB: 20% of subjects were used for fine-tuning and 70% were kept for testing, with no frozen layers. On the official VitalDB test subset,

after conservative ECG quality filtering, the model achieved a waveform MAE of 13.10 mmHg, with SBP 15.84 mmHg and DBP 10.42 mmHg. Although still above clinical thresholds, these values are comparable to other calibration-free approaches summarized in Table III.

TABLE III
CALIBRATION-FREE BP ESTIMATION PERFORMANCE REPORTED IN PRIOR WORKS USING DATASETS WITH RELIABLE SUBJECT SEPARATION.

Citation	SBP (MAE ± SDE)	DBP (MAE ± SDE)
Aguirre et al. [41]	14.39 ± 17.87	6.57 ± 8.43
Slapnicar et al. [42]	$15.41\pm$ –	$12.38\pm$ –
This work	15.84 ± 13.46	10.42 ± 7.75

These results highlight the difficulty of cross-database generalization but also the adaptability of the proposed framework. Figure 3 shows an example of the predicted volumetric flow $Q(t)$ at the fingertip (x=1). Although no ground truth for Q was available during training, the predicted waveform exhibits physiologically plausible morphology, indicating that the physics constraints guide the latent flow variable toward hemodynamically consistent solutions.

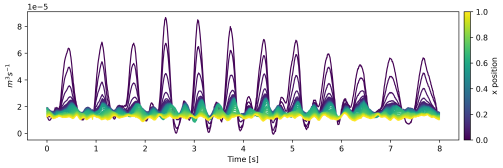

Fig. 3. Example of the predicted volumetric flow $Q(t)$ at the fingertip (x=1). No ground truth for Q was used during training; the physically consistent waveform emerges from the PDE and Windkessel constraints.

X. RESULTS DISCUSSION

The results reinforce a widely acknowledged limitation in cuffless blood pressure estimation: ECG and PPG alone are insufficient for accurate, calibration-free BP prediction [18], [27], [28]. Even when physiological constraints are embedded through a PINN, the intrinsic degeneracy between distal waveforms and central pressure cannot be fully resolved. At the same time, physics-informed modeling improves interpretability, stability, and robustness, making the framework more informative than a purely black-box regressor.

From a quantitative standpoint, the proposed method achieves calibration-free performance comparable to established baselines on VitalDB [43]. Across studies, systolic and diastolic MAEs under strict subject-disjoint evaluation typically fall in the ranges of about 9–16 mmHg and 5–12 mmHg, respectively, indicating that the proposed PINN operates within the current state of the field.

Qualitatively, the model produces physiologically plausible pressure and flow dynamics along the arterial axis. As shown in Figure 4, predicted systolic and diastolic pressures decrease progressively from the aorta to the fingertip. At the waveform level, Figure 5 shows that systolic and diastolic phases are well reproduced, with the main discrepancies concentrated around the dicrotic notch.

A. Identifiability and observational constraints

A fundamental limitation of the proposed approach is the partially under-constrained nature of the inverse hemodynamic problem. ECG and fingertip PPG provide indirect and spatially localised observations of the arterial state: ECG captures the cardiac electrical cycle rather than the mechanical ejection directly, while PPG reflects pulsatile blood volume at a single peripheral site. Different parameter sets $\boldsymbol{\theta}$ can therefore produce similar peripheral waveform morphologies.

The framework mitigates this degeneracy through three complementary mechanisms retained in the final manuscript. First, soft physiological priors restrict the parameter search space to plausible ranges. Second, the Windkessel boundary condition adds a terminal pressure–flow constraint beyond the interior PDE. Third, spatial collocation enforces consistency of the predicted fields across the full vessel axis $x \in [0, 1]$, rather than only at the supervised observation point.

Despite these mechanisms, the identifiability problem is not fully resolved. The performance drop from intra-database (MAE 5.77 mmHg) to cross-database (MAE 13.10 mmHg) is consistent with this limitation under distributional shift and suggests that additional subject-specific information will be required.

B. Scope of the calibration-free claim

Here, *calibration-free* means that no per-subject cuff BP reference is required at deployment. The model is applied to unseen subjects from ECG/PPG morphology alone, unlike methods requiring an initial cuff anchor [18]. The 20% VitalDB fine-tuning should be read astarget-domain adaptation, not per-subject calibration, since no cuff reference from test subjects is used.

This claim does not imply universal robustness: fingertip PPG captures only local distal hemodynamics and cannot represent long-term changes in vascular tone, hydration, posture, or autonomic state. The results should therefore be interpreted as proof of concept rather than evidence of clinical-grade robustness.

C. Limitations of the simplified 1D hemodynamic model

The 1D model is tractable and interpretable, but it neglects key anatomical features of the real arterial tree that may introduce systematic modelling errors.

Arterial bifurcations. The true arterial system is a branching network, whereas our formulation collapses it into a single equivalent path with Windkessel termination. As a result, bifurcation-specific reflection patterns are not represented explicitly.

Vessel curvature and non-planarity. The governing equations assume a straight, axisymmetric conduit, so curvature-induced secondary-flow effects are neglected.

Localised stenosis and focal stiffening. Local pathology may generate pressure drops and central-pressure differences that are not recoverable from peripheral morphology alone. Critically, individuals with atherosclerotic lesions may produce PPG waveforms qualitatively similar to healthy subjects

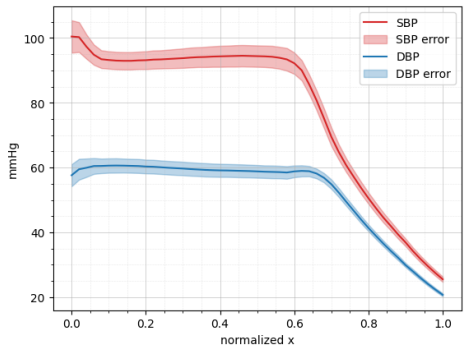

Fig. 4. Example of the SBP and DBP prediction and their respective uncertainties from aorta (x=0) and fingertip (x=1).

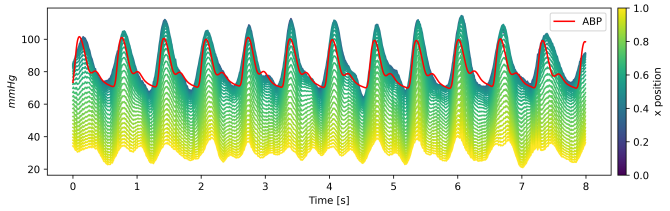

Fig. 5. Example of the ABP prediction from aorta (x=0) and fingertip (x=1). In red the real ground truth of the ABP.

while having significantly different underlying BP states — a fundamental ambiguity that no single-path peripheral model can resolve without additional subject specific information.

These omissions may bias predictions in subjects with strong peripheral reflections or vascular pathology. A natural next step is a multi-segment representation with explicit bifurcation matching conditions.

D. Clinical context, ISO 81060-2, and deployment roadmap

To contextualise the reported results with respect to established clinical standards, we compare our performance against ISO 81060-2 [16]. The standard requires a mean error within 5 mmHg and a standard deviation within 8 mmHg for both SBP and DBP. Our VitalDB results (SBP 15.84 mmHg $\pm$ 13.46, DBP 10.42 mmHg $\pm$ 7.75) remain well above that threshold, consistent with the broader difficulty of calibration-free subject-disjoint BP estimation. The proposed method is therefore not ISO 81060-2 compliant and should not be considered clinically deployable.

Closing this gap will likely require richer subject-specific inputs such as metadata, multi-site sensing, and vascular stiffness proxies [41]. These additions would better constrain the inverse problem and reduce the remaining degeneracy.

Real-time and embedded deployment. The current model was validated offline. Its size is compatible with embedded inference, but automatic differentiation for PDE residuals is not. A practical route is therefore to train the full PINN offline, freeze the inference network, and deploy only the forward pass through TensorFlow Lite or ONNX, with the physics constraints enforced implicitly through the learned weights rather than explicitly at runtime.

XI. Conclusion

This work presented a heart-to-finger hemodynamic Physics-Informed Neural Network (PINN) for cuffless arterial blood pressure waveform estimation from ECG and PPG signals. The main findings can be summarized across the neural-network, physics-informed, and cross-database aspects of the study.

Neural network findings. The proposed architecture learns to solve an inverse hemodynamic problem rather than a direct ECG/PPG-to-BP regression. Through the parameter layer, the model infers subject-window-specific hemodynamic scalars that govern the 1D PDE system, allowing the prediction head to generate physically consistent pressure and flow fields. On the held-out MIMIC-III test set, the model achieved a waveform MAE of 5.77 mmHg (SBP 7.32 mmHg, DBP 5.12 mmHg). Beyond the BP waveform itself, the framework also reconstructs latent physiological quantities such as flow, compliance, wall stiffness, and spatial pressure evolution.

Physics-informed modelling findings. The composite loss enforces physiological consistency through ABP supervision, distal PPG anchoring, PDE residuals, Windkessel boundary conditions, and soft physiological priors. These constraints reduce non-physical solutions and preserve realistic proximal-to-distal pressure attenuation and waveform structure, while keeping the model interpretable and more stable than a purely black-box alternative.

Cross-database generalisation. When transferred directly from MIMIC-III to VitalDB, performance degraded to a waveform MAE of 17.02 mmHg, reflecting the expected distributional shift between the two datasets. After limited fine-tuning on 20% of VitalDB subjects, performance improved to a waveform MAE of 13.10 mmHg (SBP 15.84 mmHg, DBP 10.42 mmHg), comparable to current calibration-free baselines under subject-disjoint evaluation. This confirms that physics-informed constraints help adaptation, but also that the ECG/PPG-to-BP inverse problem remains only partially identifiable without richer subject-specific information.

Current limitations and path forward. The results do not satisfy ISO 81060-2 and the method is not clinically deployable in its current form, as expected for a proof-of-concept study. The main limitations are the identifiability gap associated with sparse observations, the simplifications of the 1D single-path model, and the lack of subject-specific descriptors anchoring the inferred parameters to individual physiology. Future progress will likely require demographic metadata, multi-site PPG, vascular-stiffness surrogates, and more expressive vascular representations, moving the framework toward more robust and physiologically grounded calibration-free BP monitoring.

References

[1] F. D. Fuchs and P. K. Whelton, "High blood pressure and cardiovascular disease," *Hypertension*, vol. 75, no. 2, pp. 285–292, 2020.
[2] N. Pilz, D. Picone, A. Patzak, O. Opatz, T. Lindner, L. Fesseler, V. Heinz, and T. Bothe, "Cuff-based blood pressure measurement: challenges and solutions," *Blood Pressure*, vol. 33, no. 1, p. 2402368, 2024.
[3] M. Nour, K. Polat, Ü. Şentürk, and M. Arıcan, "A novel cuffless blood pressure prediction: uncovering new features and new hybrid ml models," *Diagnostics*, vol. 13, no. 7, p. 1278, 2023.

[4] F. Delrio, V. De Vitis, S. Caligari, V. Randazzo, G. Cirrincione, and E. Pasero, "Enhancing ecg analysis with a hybrid deep learning approach: Automatic detection of significant features," in *Advanced Neural Artificial Intelligence: Theories and Applications*, pp. 23–33, Springer, 2025.

[5] V. Randazzo, J. Ferretti, and E. Pasero, "Anytime ECG monitoring through the use of a low-cost, user-friendly, wearable device," vol. 21, no. 18, p. 6036.

[6] J. Ferretti, V. Randazzo, G. Cirrincione, and E. Pasero, "1-D convolutional neural network for ECG arrhythmia classification," in *Progresses in Artificial Intelligence and Neural Systems* (A. Esposito, M. Faundez-Zanuy, F. C. Morabito, and E. Pasero, eds.), Smart Innovation, Systems and Technologies, pp. 269–279, Springer.

[7] F. Delrio, V. Randazzo, G. Cirrincione, and E. Pasero, "Non-invasive arterial blood pressure estimation from electrocardiogram and photoplethysmography signals using a conv1d-bilstm neural network," *Engineering Proceedings*, vol. 39, no. 1, p. 78, 2023.

[8] A. Paviglianiti, V. Randazzo, G. Cirrincione, and E. Pasero, "Neural recurrent approches to noninvasive blood pressure estimation," in *2020 international joint conference on neural networks (IJCNN)*, pp. 1–7, IEEE, 2020.

[9] S. N. A. Ismail, N. A. Nayan, R. Jaafar, and Z. May, "Recent advances in non-invasive blood pressure monitoring and prediction using a machine learning approach," vol. 22, no. 16, p. 6195.

[10] V. Randazzo, P. Buccellato, J. Ferretti, F. Delrio, and E. Pasero, "Pulsecg-a cuffless non-invasive blood pressure monitoring device through neural network analysis of ecg and ppg signals," in *2024 IEEE 22nd Mediterranean Electrotechnical Conference (MELECON)*, pp. 1030–1035, IEEE, 2024.

[11] Z. Lou, J. Tao, B. Wei, X. Jiang, S. Cheng, Z. Wang, C. Qin, R. Liang, H. Guo, L. Zhu, *et al.*, "Near-infrared organic photodetectors toward skin-integrated photoplethysmography-electrocardiography multimodal sensing system," *Advanced Science*, vol. 10, no. 36, p. 2304174, 2023.

[12] G. Cirrincione, V. Randazzo, and E. Pasero, "A neural based comparative analysis for feature extraction from ECG signals," in *Neural Approaches to Dynamics of Signal Exchanges* (A. Esposito, M. Faundez-Zanuy, F. C. Morabito, and E. Pasero, eds.), Smart Innovation, Systems and Technologies, pp. 247–256, Springer.

[13] V. Randazzo, G. Marchetti, C. Giustetto, E. Gugliermina, R. Kumar, G. Cirrincione, F. Gaita, and E. Pasero, "Learning-based approach to predict fatal events in brugada syndrome," in *Applications of Artificial Intelligence and Neural Systems to Data Science*, pp. 63–72, Springer, 2023.

[14] G. Cirrincione, V. Randazzo, and E. Pasero, "The growing curvilinear component analysis (gcca) neural network," *Neural Networks*, vol. 103, pp. 108–117, 2018.

[15] L. Zhao, C. Liang, Y. Huang, G. Zhou, Y. Xiao, N. Ji, Y.-T. Zhang, and N. Zhao, "Emerging sensing and modeling technologies for wearable and cuffless blood pressure monitoring," *npj Digital Medicine*, vol. 6, no. 1, p. 93, 2023.

[16] R. Mukkamala, M. Yavarimanesh, K. Natarajan, J.-O. Hahn, K. G. Kyriakoulis, A. P. Avolio, and G. S. Stergiou, "Evaluation of the accuracy of cuffless blood pressure measurement devices: challenges and proposals," *Hypertension*, vol. 78, no. 5, pp. 1161–1167, 2021.

[17] S. Zhou, L. Xu, L. Hao, H. Xiao, Y. Yao, L. Qi, and Y. Yao, "A review on low-dimensional physics-based models of systemic arteries: application to estimation of central aortic pressure," *Biomedical engineering online*, vol. 18, no. 1, p. 41, 2019.

[18] R. Mukkamala, G. S. Stergiou, and A. P. Avolio, "Cuffless blood pressure measurement," *Annual Review of Biomedical Engineering*, vol. 24, no. 1, pp. 203–230, 2022.

[19] Guo, Cheng-Yan and Huang, Chi-Hung and Chang, Chia-Chi and Wang, Kuan-Jen and Hsieh, Tung-Li, "Combining local PWV and quantified arterial changes for calibration-free cuffless blood pressure estimation: a clinical validation," *IEEE Sensors Journal*, vol. 23, no. 1, pp. 658–668, 2022.

[20] Xu, Qianwen and Dragicevic, Tomislav and Xie, Lihua and Blaabjerg, Frede, "Artificial Intelligence-Based Control Design for Reliable Virtual Synchronous Generators," *IEEE Transactions on Power Electronics*, vol. 36, no. 8, pp. 9453–9464, 2021.

[21] Li, Chao and Yang, Yongheng and Blaabjerg, Frede, "Mechanism Analysis for Oscillation Transferring in Grid-Forming Virtual Synchronous Generator Connected to Power Network," *IEEE Transactions on Industrial Electronics*, 2025. doi: 10.1109/TIE.2025.3531473.

[22] Wang, Yuan and Zhao, Xu and He, Liang and Zhen, Zhen and Chen, Hao, "ContractGNN: Ethereum Smart Contract Vulnerability Detection Based on Vulnerability Sub-Graphs and Graph Neural Networks," *IEEE Transactions on Network Science and Engineering*, 2024. doi: 10.1109/TNSE.2024.3470788.

[23] F. Delrio, V. Randazzo, G. Cirrincione, and E. Pasero, "Physics informed neural network for continuous and cuffless arterial blood pressure," in *2025 IEEE International Conference on Artificial Intelligence for Learning and Optimization (ICoAILO)*, pp. 143–148, IEEE, 2025.

[24] A. Paviglianiti, V. Randazzo, S. Villata, G. Cirrincione, and E. Pasero, "A comparison of deep learning techniques for arterial blood pressure prediction," vol. 14, no. 5, pp. 1689–1710.

[25] Attivissimo, Filippo and De Palma, Luisa and Di Nisio, Attilio and Scarpetta, Marco and Lanzolla, Anna Maria Lucia, "Photoplethysmography signal wavelet enhancement and novel features selection for non-invasive cuff-less blood pressure monitoring," *Sensors*, vol. 23, no. 4, p. 2321, 2023.

[26] Hasanzadeh, Navid and Ahmadi, Mohammad Mahdi and Mohammadzade, Hoda, "Blood pressure estimation using photoplethysmogram signal and its morphological features," *IEEE Sensors Journal*, vol. 20, no. 8, pp. 4300–4310, 2019.

[27] R. Yoshizawa, K. Yamamoto, and T. Ohtsuki, "Investigation of data leakage in deep-learning-based blood pressure estimation using photoplethysmogram/electrocardiogram," *IEEE Sensors Journal*, vol. 23, no. 12, pp. 13311–13318, 2023.

[28] S. Mehta, N. Kwatra, M. Jain, and D. McDuff, "Examining the challenges of blood pressure estimation via photoplethysmogram," *Scientific Reports*, vol. 14, no. 1, p. 18318, 2024.

[29] M. Raissi, P. Perdikaris, and G. E. Karniadakis, "Physics-informed neural networks: A deep learning framework for solving forward and inverse problems involving nonlinear partial differential equations," *Journal of Computational physics*, vol. 378, pp. 686–707, 2019.

[30] N. Westerhof, J.-W. Lankhaar, and B. E. Westerhof, "The arterial windkessel," *Medical & biological engineering & computing*, vol. 47, no. 2, pp. 131–141, 2009.

[31] L. Li, X.-C. Tai, and R. H.-F. Chan, "A new method to compute the blood flow equations using the physics-informed neural operator," *Journal of Computational Physics*, vol. 519, p. 113380, 2024.

[32] K. Sel, A. Mohammadi, R. I. Pettigrew, and R. Jafari, "Physics-informed neural networks for modeling physiological time series for cuffless blood pressure estimation," *npj Digital Medicine*, vol. 6, no. 1, p. 110, 2023.

[33] H. Crandall *et al.*, "Cuffless, calibration-free hemodynamic monitoring with physics-informed machine learning models," 2025. arXiv:2601.00081.

[34] D. N. Ku, "Blood flow in arteries," *Annual review of fluid mechanics*, vol. 29, no. 1, pp. 399–434, 1997.

[35] A. R. Pries, D. Neuhaus, and P. Gaehtgens, "Blood viscosity in tube flow: dependence on diameter and hematocrit," *American Journal of Physiology-Heart and Circulatory Physiology*, vol. 263, no. 6, pp. H1770–H1778, 1992.

[36] A. S. Olufsen, "Modeling the arterial system with reference to an anesthesia simulator," 1998.

[37] G. Langewouters, K. Wesseling, and W. Goedhard, "The static elastic properties of 45 human thoracic and 20 abdominal aortas in vitro and the parameters of a new model," *Journal of biomechanics*, vol. 17, no. 6, pp. 425–435, 1984.

[38] S. Chen, S. Fan, Z. Qiao, Z. Wu, B. Lin, Z. Li, M. A. Riegler, M. Y. H. Wong, A. Opheim, O. Korostynska, *et al.*, "Transforming healthcare: Intelligent wearable sensors empowered by smart materials and artificial intelligence," *Advanced Materials*, p. 2500412, 2025.

[39] D. Taylor, "Blood flow in arteries. by da mcdonald. edward arnold, london, 1974. pp. xviii+ 496.£ 12," *Quarterly Journal of Experimental Physiology and Cognate Medical Sciences: Translation and Integration*, vol. 60, no. 1, pp. 65–65, 1975.

[40] J. Lighthill, "The mechanics of the circulation. by cg caro, tj pedley, rc schroter and wa seed. oxford university press, 1978. 527 pp.£ 22.00 (hardback) or£ 11.00 (paperback).," *Journal of Fluid Mechanics*, vol. 90, no. 4, pp. 794–797, 1979.

[41] N. Aguirre, E. Grall-Maës, L. J. Cymberknop, and R. L. Armentano, "Blood pressure morphology assessment from photoplethysmogram and demographic information using deep learning with attention mechanism," *Sensors*, vol. 21, no. 6, p. 2167, 2021.

[42] G. Slapničar, N. Mlakar, and M. Luštrek, "Blood pressure estimation from photoplethysmogram using a spectro-temporal deep neural network," *Sensors*, vol. 19, no. 15, p. 3420, 2019.

[43] H.-C. Lee, Y. Park, S. B. Yoon, S. M. Yang, D. Park, and C.-W. Jung, "Vitaldb, a high-fidelity multi-parameter vital signs database in surgical patients," *Scientific Data*, vol. 9, no. 1, p. 279, 2022.